Chinese Chemical Letters 36 (2025) 110672

Contents lists available at ScienceDirect

Chinese Chemical Letters

journal homepage: www.elsevier.com/locate/cclet

Multidimensional droplet manipulation on superhydrophobic surfaces using acoustic tweezers

Guifeng Wen, Zheyuan Zhong, Yue Fan, Xuelin Tian, Shilin Huang*

School of Materials Science and Engineering, Key Laboratory for Polymeric Composite & Functional Materials of Ministry of Education, Sun Yat-sen University, Guangzhou 510006, China

ARTICLE INFO

Article history:
Received 2 September 2024
Revised 14 November 2024
Accepted 22 November 2024
Available online 24 November 2024

Keywords:
Superhydrophobic surfaces
Acoustic tweezers
Droplet manipulation
Microfluidics
Micro-reactions

ABSTRACT

On-demand droplet manipulation plays a critical role in microfluidics, bio/chemical detection and micro-reactions. Acoustic droplet manipulation has emerged as a promising technique due to its non-contact nature, biocompatibility and precision, circumventing the complexities associated with other methods requiring surface or droplet pretreatment. Despite their promise, existing methods for acoustic droplet manipulation often involve complex hardware setups and difficulty for controlling individual droplet amidst multiple ones. Here we fabricate simple yet effective acoustic tweezers for in-surface and out-of-surface droplet manipulation. It is found that droplets can be transported on the superhydrophobic surfaces when the acoustic radiation force surpasses the friction force. Using a two-axis acoustic tweezer, droplets can be maneuvered along arbitrarily programmed paths on the surfaces. By introducing multiple labyrinthine structures on the superhydrophobic surface, individual droplet manipulation is realized by constraining the unselected droplets in the labyrinthine structures. In addition, a three-axis acoustic tweezer is developed for manipulating droplets in three-dimensional space. Potential applications of the acoustic tweezers for micro-reaction, bio-assay and chemical analysis are also demonstrated.

Droplet manipulation is indispensable in various application fields, encompassing microfluidics [1–3], bio/chemical detection [4–6], heat transfer [7,8], and micro-reaction [9,10]. Various external stimuli, such as electric fields, magnetic fields, light and sound, have been employed for droplet manipulation [11–21]. Among these techniques, electric fields are most commonly used since they enable precise and complex droplet operations (*e.g.*, dispensing, transporting, mixing and splitting); however, they require intricate electrode designs and relatively high voltages, which may adversely affect biological samples [1,22]. Magnetic fields allow remote and non-contact control of droplets, but they usually necessitate the addition of magnetic particles to the manipulated droplets, which may cause unwanted contamination [23]. Light provides excellent spatial and temporal resolution for non-contact droplet manipulation, though it often requires bulky optics and may induce heating in droplets [13,24]. Recently, acoustic manipulation has emerged as a highly promising method for droplet manipulation, since it provides a contactless, non-invasive, highly biocompatible and precise method of controlling droplets, eliminating the necessity for surface or droplet pretreatment, a challenge often encountered with other manipulation techniques [25,26].

There are two methods to manipulate droplets in air using acoustic fields. The first method involves the utilization of surface acoustic waves, which are mechanical waves propagating along the surfaces of piezoelectric substrates, typically with micrometer-scale wavelengths [27–29]. These waves are generated by interdigital transducers and can be highly localized on the surfaces, enabling precise manipulation of droplets. However, employing surface acoustic waves for droplet manipulation in air poses challenges such as heat generation and the intricate fabrication of the interdigital electrodes on the piezoelectric substrates. The second method entails the construction of mid-air acoustic tweezers (ATs), which are created and regulated by ultrasonic transducers [25,26,30,31]. For instance, Yuan *et al.* developed an AT utilizing an ultrasonic phased array for versatile droplet manipulation on superhydrophobic surfaces (SHPSs) [26]. The AT generated a twin trap ultrasonic field, enabling the trapping and manipulation of droplets without the need for surface or droplet pretreatment. It was used to translate the droplets along programmed paths, pass through narrow slits and traverse steep slopes, providing a com-

* Corresponding author.
E-mail address: huangshlin@mail.sysu.edu.cn (S. Huang).

https://doi.org/10.1016/j.cclet.2024.110672
1001-8417/

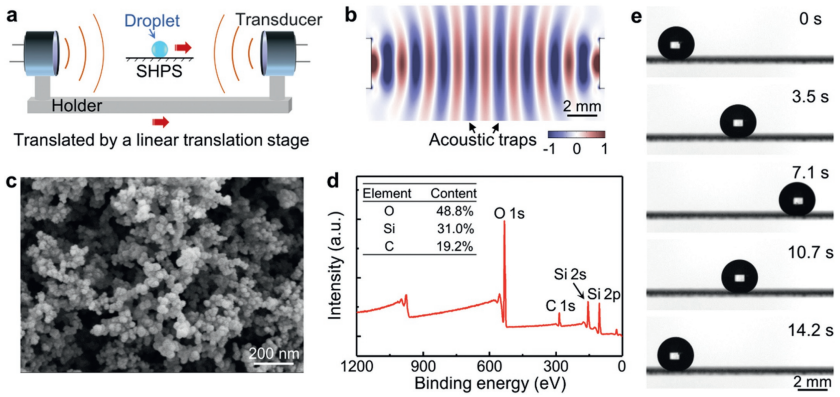

Fig. 1. (a) Schematic diagram of the single-axis AT consisting of a pair of ultrasonic transducers. (b) Distribution of Gor'kov potential in the single-axis AT. The potential is normalized by the maximal potential. (c) Scanning electron microscopy image of the superhydrophobic coating. (d) X-ray photoelectron spectroscopy wide scan spectrum of the superhydrophobic coating. (e) Photographs showing the transportation of a 5-μL water droplet following the motion of the AT.

prehensive platform for contactless and programmable droplet manipulation. In another study by Luo *et al.*, a simple yet effective contactless AT was devised for droplet manipulation on SHPSs, leveraging ultrasonic standing waves between an ultrasonic transducer and the surface to manipulate droplets without physical contact [25]. Through adjustments to the transducer, this AT was capable of levitating small droplets (0.6–21 μL) for out-plane manipulation and trapping large droplets (5–500 μL) for in-plane manipulation on various SHPSs.

Although ATs have been employed to manipulate droplets on SHPSs, several limitations still persist. These include the need for relatively complex hardware and software setup [26], as well as restrictions on transporting small droplets (<5 μL) on the SHPSs [25]. In addition, it is challenging to individually manipulate a droplet among multiple ones due to the unintended influence of the acoustic field on the other droplets. Finally, the capability of using AT to transport droplets off the SHPSs and guide them along arbitrary trajectories in three-dimensional (3D) space requires further exploration.

Here, we present the development of simple ATs for multidimensional manipulation of droplets. It is revealed that the droplets on the SHPSs can be maneuvered by the ATs when the acoustic radiation force surpasses the friction force. ATs consisting of two pairs of orthogonal ultrasonic transducers can be used to precisely transport droplets on the SHPS along arbitrarily programmed paths. These droplets can be mixed as needed when they are transported to a designated pinning spot on the SHPS. By incorporating distinct labyrinthine structures on the SHPS for local constraint of droplets, the AT can also be used to selectively deliver individual droplets among multiple ones. Finally, a three-axis AT is built for 3D manipulation of droplets off the SHPS, enabling capture, transport, release and mixing of droplets. This study sheds light on the working principles of acoustic tweezers, and offers tools for multidimensional droplet manipulation.

The single-axis AT is schematically depicted in Fig. 1a. It consists of a pair of circular ultrasonic transducers (each 10 mm in diameter) arranged horizontally in a coaxial configuration and secured with a 3D-printed plastic holder. The ultrasonic transducers are simultaneously driven by a 40 kHz square-wave electric signal using a function generator and a power amplifier (see Experimental section and Fig. S1 in Supporting information for detailed illustrations of the equipment). This results in two counter-propagating acoustic waves with identical amplitude and phase propagating along opposing directions, the superposition of which generates an acoustic standing wave. For a small sphere with a radius of R located in the acoustic field, the potential for the acoustic radiation force (U_{ac}, also called Gor'kov potential) can be calculated using the Gor'kov expression (Eq. 1) [32,33]:

$$U_{ac} = 2\pi R^3 \left[\frac{f_1}{3\rho_0 {c_0}^2} \langle p^2 \rangle - \frac{f_2 \rho_0}{2} \langle u^2 \rangle \right] \quad (1)$$

where p and u denote the sound pressure and particle velocity, respectively. The coefficients f_1 and f_2 depend on the densities (ρ_0, ρ_s) and sound velocities (c_0, c_s) of the medium and sphere, with $f_1 = 1 - \frac{\rho_0 {c_0}^2}{\rho_s {c_s}^2}$ and $f_2 = 2\frac{\rho_s - \rho_0}{2\rho_s + \rho_0}$. For a sphere in mid-air, since its density is much larger than that of air, both f_1 and f_2 equal 1. Using COMSOL Multiphysics software, we simulated the pressure and particle velocity distributions within the acoustic field and subsequently calculated the radiation force potential using Eq. 1. Fig. 1b and Fig. S2 (Supporting information) show the potential distribution in a single-axis AT setup with an inter-transducer spacing of 36 mm. Multiple potential wells are evident in the AT, exhibiting bilateral symmetry with respect to the center vertical axis. These potential wells are separated by approximately 4.3 mm, which is half of the wavelength ($\lambda = c_0/f$, where $c_0 = 343$ m/s and $f = 40$ kHz) of the mid-air acoustic wave. These potential wells serve as acoustic traps for manipulating droplets. To allow transportation of droplets on the SHPS, the single-axis AT is horizontally translated using a linear translation stage, and the SHPS is positioned between the transducers, aligning its top surface at the same height as the horizontal symmetric axis of the ultrasonic transducers. This setup ensures that acoustic waves can effectively transmit to the droplet on the SHPS without obstruction by the SHPS. The scanning electron microscopy image in Fig. 1c reveals that the SHPS has a porous surface structure with stacked nanoparticles. The X-ray photoelectron spectroscopy spectrum (Fig. 1d) shows that the surface is predominantly comprised of Si (31.0%), O (48.8%), and C (19.2%), consistent with NeverWet's composition reported in literature—silica nanoparticles coated with poly(siloxane) [34]. The nanoscale roughness and low surface energy components (poly(siloxane)) contribute to the superhydrophobic property, and the friction of water droplet on the SHPS can be effectively decreased due to the persistence of air cushion at the SHPS-water interface [35,36]. The static contact angle of water on the SHPS reaches 166° ± 5°, and the sliding angle for a 5-μL droplet is only 1.5° ± 0.8°. The single-axis AT can trap droplets in the potential wells, enabling droplet transportation when the AT is translated. As shown in Fig. 1e, Fig. S3 and Movie S1 (Supporting information), when the AT under a voltage of 25 V is translated at a constant velocity of 1 mm/s, a 5-μL water droplet on the SHPS is smoothly transported at the same velocity. When the voltage is decreased to 10 V (Fig. S3), the trapping force is weakened. As a result, the droplet exhibits an intermittent moving behavior. Further reducing

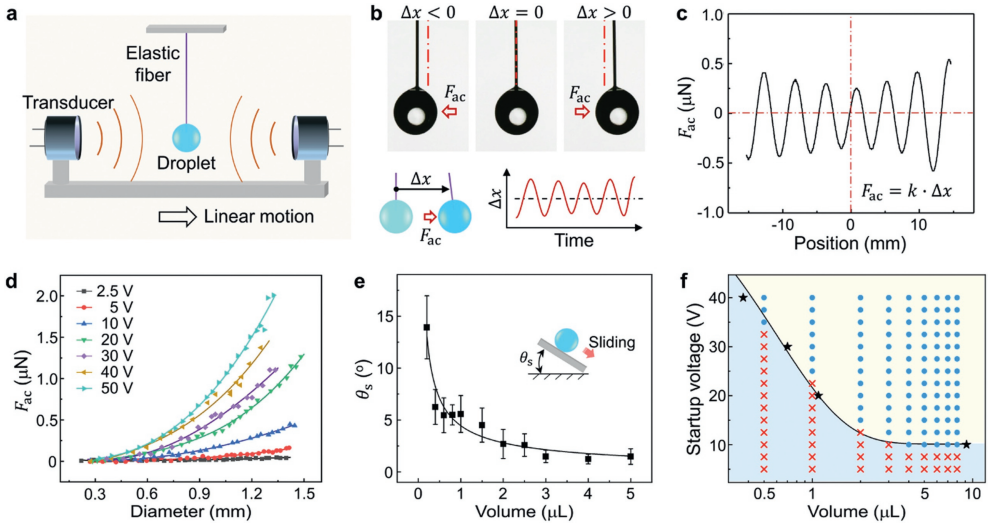

Fig. 2. (a) Schematic diagram showing the force sensor used to measure the acoustic radiation force acting on the droplet in the single-axis AT setup. (b) Photographs showing the deflection of the elastic fiber when the attached droplet is subjected to the acoustic radiation force F_{ac}. The deflection is defined as the displacement of the lower end of the elastic fiber. (c) The acoustic radiation force acting on the droplet along the horizontal symmetric axis of the AT. (d) The acoustic radiation forces acting on the droplets as functions of droplet diameter. (e) The sliding angles of water droplets with different volumes on the SHPS. (f) Regime diagram for acoustic droplet transportation on SHPS. The solid curve represents the predicted start-up voltages for transporting the droplets.

the applied voltage to 5 V leads to failure in droplet transportation using the AT. This voltage-dependent behavior in droplet transportation will be explored in more detail below.

To investigate the mechanism of acoustic droplet transportation on the SHPS, the acoustic radiation force acting on the droplet should be measured. As shown in Fig. 2a, a thin elastic fiber is used as the force sensor to measure the acoustic radiation force acting on the droplet [37–40]. The elastic fiber (diameter = 0.1 mm, length = 68 mm) is vertically aligned and secured at its top end by a plastic holder. The droplet is suspended at the lower end of the elastic fiber, positioned at the same height as the horizontal symmetric axis of the ultrasonic transducers. Once the droplet is subjected to the acoustic radiation force, the elastic fiber gets deflected by a distance of Δx (Fig. 2b). At equilibrium, the acoustic radiation force is counteracted by the restoring force which is proportional to Δx. The acoustic radiation force F_{ac} acting on the droplet can be calculated as follows (Eq. 2):

$$F_{ac} = k\Delta x \tag{2}$$

where the elastic constant k is calibrated using a force balance with high accuracy, detailed in Fig. S4 and Experimental section (Supporting information) [39,41]. One example of the acoustic radiation force acting on the droplet is presented in Fig. 2c, showing undulating changes of the force along the horizontal symmetric axis of the single-axis AT. At the center of the AT, the acoustic radiation force approaches zero. Deviation from the center would induce forces guiding the droplet to nearby potential wells (U_{ac} reaching local minimal while $F_{ac} = 0$, Fig. S2). On the other hand, departure from the center of a potential well would prompt a restoring force that directs the droplet back to the well center. Fig. 2c and Fig. S2 also show that the amplitude of the acoustic radiation force becomes larger when approaching the transducers, reflecting a stronger acoustic field near the transducers.

The acoustic radiation force is not only influenced by the relative position of the droplet in the acoustic field, but also by the droplet size and the applied voltage. To study the influence of droplet size on the acoustic radiation force, the droplet attached to the elastic fiber was allowed to evaporate, and the resulting acoustic radiation force on the droplet with a decreasing volume was determined. As shown in Fig. 2d, decreasing the droplet diameter correlates with the reduction in acoustic radiation force (the force amplitude around the center of the AT). This agrees well with the expectation that the acoustic radiation force is proportional to the cube of droplet diameter [32]. Furthermore, the acoustic radiation force can be tuned by the applied voltage. Applying a higher voltage increases the acoustic strength, consequently enhancing the acoustic radiation force acting on the droplet. This explains the results given in Fig. S3, which demonstrates that a higher voltage is beneficial for acoustic manipulation of the droplet.

To transport a droplet on the SHPS, the friction force acting on the droplet should be overcome. The friction force can be quantified by measuring the sliding angle (α) of the droplet, which is the critical tilt angle at which the gravitational force acting on the droplet became sufficient to overcome the friction force ($f_s = \rho V g \sin\alpha$, where f_s is the friction force, V is the droplet volume and g is the gravitational acceleration). It can be further deduced that the friction force is correlated with droplet volume following Eq. 3:

$$f_s = \rho g V^{1/3} B \tag{3}$$

where $B = \frac{k\gamma}{\rho g}\sqrt[3]{\frac{24\sin^3\theta}{\pi(1-\cos\theta)^2(2+\cos\theta)}}(\cos\theta_{rec} - \cos\theta_{adv})$, which is determined by the geometric factor k, the droplet surface tension γ, the static contact angle θ, the advancing contact angle (θ_{adv}) and receding contact angle (θ_{rec}) of the droplet on the surface. A detailed derivation of Eq. 3 and a discussion on how contact angle and contact angle hysteresis influence the friction force can be found in supplementary discussion and Fig. S5 (Supporting information). The experimental results in Fig. 2e are fitted using Eq. 3 to obtain B (here $B = 0.0776\ \mu L^{2/3}$), enabling the prediction of the friction force f_s for a droplet with a volume of V.

It can be hypothesized that once the acoustic radiation force is able to overcome the friction force, the droplet can be transported on the SHPS using the AT. In Fig. S6 (Supporting information), we overlay the $F_{ac} \sim V$ and $f_s \sim V$ curves and identify the critical volume at which the acoustic radiation force equals the friction force at a given voltage. It is evident that with increasing the applied voltage, the critical volume becomes smaller, meaning that a stronger AT is requisite to manipulate relatively small droplets. Conversely, for droplets with the same volume, there exists a critical voltage (called start-up voltage) at which the acoustic radiation force equals the friction force. The deduced start-up voltage

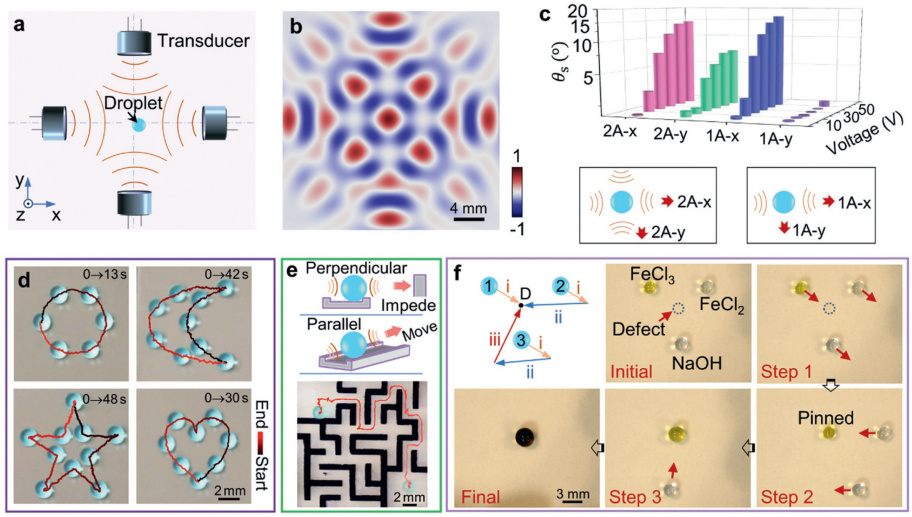

Fig. 3. (a) Schematic diagram of the two-axis AT setup. (b) Distribution of the Gor'kov potential for the two-axis AT. The potential is normalized by the maximal potential. (c) Sliding angles of 2-μL droplets on the SHPS when different voltages are applied to generate the two-axis and single-axis (abbreviated as 2A and 1A) acoustic fields. (d) Time-lapsed images showing the motion of the droplet driven by the two-axis AT. (e) Using the two-axis AT to transport a droplet in the labyrinth. (f) Micro-reaction realized by the two-axis AT.

is depicted in Fig. 2f (star points and solid curve), showing a decreasing tendency with increasing droplet volume. Indeed, experimental observations confirm that droplets can only be successfully transported when the applied voltage exceeds the deduced start-up voltage (circle: able to transport; cross: unable to transport). This verifies the fact that for successful transportation of droplets on the SHPS using a AT, the acoustic radiation force should surpass the friction force.

Although the single-axis AT can be used to transport droplets along the axis direction, it lacks the capability to manipulate droplets perpendicular to this axis. The two-axis AT, which is schemed in Fig. 3a and Fig. S7 (Supporting information), can generate more stable acoustic traps for 2D droplet manipulation on SHPSs. Fig. 3b illustrates the Gor'kov potential of a typical two-axis AT (inter-transducer spacing = 38.5 mm), revealing multiple potential wells (depicted in blue) around its center. These separated potential wells allow for individual trapping of droplets, restricting their movement in both the *x* and *y* directions. Fig. 3c shows that under the two-axis acoustic field, the rolling angle increased with voltage in both *x* and *y* directions, evidencing effective trapping of the droplets in both directions. In contrast, under the single-axis acoustic field, the rolling angle does not increase with voltage along the *y* direction, suggesting limited constraint of the droplet in this direction. The acoustic force distribution measured using the elastic fiber force sensor also evidences that there exist constraining forces in both *x* and *y* directions in the two-axis AT (Fig. S8, detailed experimental procedures can be found in Supporting information).

With its ability to provide trapping forces in both *x* and *y* directions, the two-axis AT is suitable for reliable in-plane 2D droplet transportation along any programed paths. For example, as shown in Fig. 3d, the droplets are transported along the circular, crescent, pentagram and heart-shaped paths using the two-axis AT (speed: 1.5 mm/s for the circular path, 0.7 mm/s for the other paths; applied voltage: 30 V). Here the two-axis AT is translated by a two-axis translation stage, enabling precise programming and control of its motion. The AT can also be manually maneuvered to realizing more complicated droplet transportation. Fig. 3e and Movie S2 (Supporting information) demonstrate the use of the two-axis AT to navigate a droplet through a labyrinth. Since the labyrinth walls (approximately 0.3 mm in height) effectively impede the droplet's movement, to move the droplet from the starting position to the destination, the AT must follow a specified path. When maneuvered manually, the two-axis AT can successfully move the droplet to the destination.

Given its multiple acoustic potential wells, the two-axis AT is able to trap and transport multiple droplets (Fig. S9 in Supporting information). However, their relative positions remain fixed during movement, making it challenging to manipulate individual droplets using only the AT. To realize individual manipulation of the droplets, SHPSs with distinct labyrinth structures can be used (Fig. S10 in Supporting information). These distinct labyrinth structures ensure that while one droplet is moved out from the labyrinth, others remain confined. This enables individual transportation of the selected droplet after being moved out from the labyrinth.

For sequential mixing of multiple droplets on the SHPS using the two-axis AT, a simple method involves creating a hydrophilic defect on the SHPS. In contact with the hydrophilic defect, the droplets would get pinned and become immobilized. Therefore, the droplets can be mixed in sequence at the pinning spot, see the top left panel in Fig. 3f. We used this routine to perform a micro-reaction. As shown in Fig. 3f and Movie S3 (Supporting information), the $FeCl_3$, $FeCl_2$ and NaOH droplets were successively translated to the defect position. The $FeCl_2$, $FeCl_3$ droplets were first mixed together resulting in a yellow mixture droplet. After adding the NaOH droplet, the mixture droplet turned black, indicating the coprecipitation of Fe(II) and Fe(III) salts under a basic condition and formation of iron oxide with black color [42]. This method can also be used for droplet-based bio-assays. For instance, in Fig. S11 (Supporting information), a transparent analyte droplet (5 mg/mL bovine serum albumin) was mixed with a droplet containing Coomassie brilliant blue (CBB) G250 using the AT. The mixture droplet uniformly turned blue after 4 min, confirming the presence of protein in the analyte droplet [43].

Apart from manipulating droplets on two-dimensional SHPSs, the acoustic fields can also be used to manipulate droplets and small particles in 3D space [32,44]. Here we present a simple yet stable 3D AT for the individual manipulation of droplets in 3D space. Figs. S12a and b (Supporting information) show digital images of the three-axis AT setup, which consists of three pairs of coaxial ultrasonic transducers arranged orthogonally with horizon-

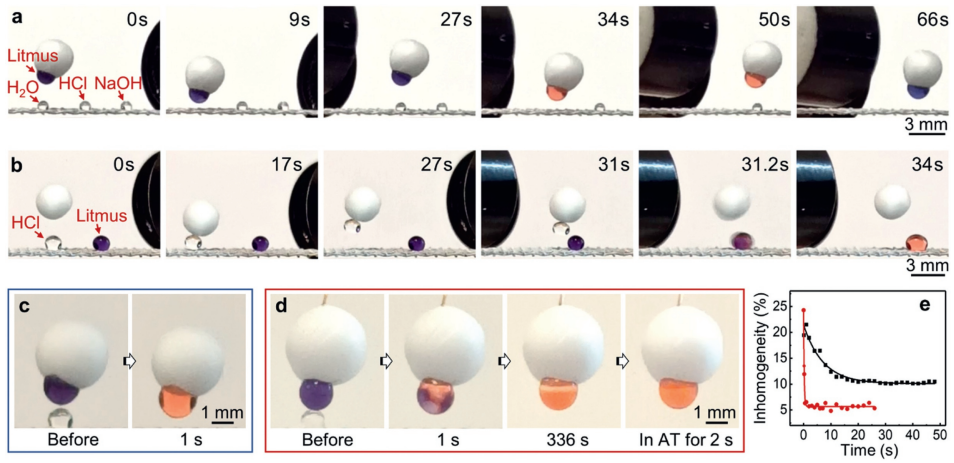

Fig. 4. (a) Using the three-axis AT to test the acid-base properties of droplets. (b) Using the three-axis AT to capture, transport, release and mix droplets. (c) Color change of the merged litmus-HCl droplet in the three-axis AT. (d) Color change of the merged litmus-HCl droplet without applying the acoustic field. (e) Evolution of color inhomogeneity for the merged droplet with and without applying the acoustic field.

tal and vertical spacings of 27 mm and 12 mm, respectively. When an electric signal (40 kHz, 35 V) is applied to the transducers, a standing acoustic field is formed in 3D space (Fig. S12c in Supporting information). Although the resulting acoustic traps (blue regions) are not strong enough to levitate the relatively heavy water droplets, it can easily levitate the expanded polystyrene (EPS) spheres. The EPS-droplet combined system can also be levitated (Figs. S12b and d in Supporting information, droplet volume: 1.5 μL, transportation speed: 16 mm/s; the EPS sphere helps to increase the acoustic radiation force for levitating the droplet). The capability to levitate the attached droplet on the EPS sphere while the unattached droplets remain static can be exploited to independently transport droplets in 3D space. As showcased in Fig. 4a and Movie S4 (Supporting information), three 1-μL droplets, *i.e.*, water, HCl (pH 1) and NaOH (pH 14) droplets, were initially deposited on a superhydrophobic mesh. The mesh structure not only impeded the lateral movement of the droplets, but also allowed efficient transmission of the acoustic waves. The three-axis AT was used to transport a litmus droplet (1.5 μL, attached to the EPS sphere) to mix with the three droplets and assessed their acid-base properties. Transported by the AT in 3D space, the purple litmus droplet was first mixed with the pure water droplet, resulting in no significant color change. Next, it was sequentially mixed with the HCl and NaOH droplets, causing its color to change to orange and blue, respectively. This demonstrates that it is feasible to use the three-axis AT to manipulate droplets individually in 3D space.

By modifying the surface of the EPS sphere, it is also possible to capture, transport, and release droplets. As depicted in Fig. 4b and Movie S5 (Supporting information), under AT manipulation, the superhydrophobic EPS sphere (coated with Glaco) successfully picked up a droplet from the superhydrophobic mesh. The droplet was then transported in 3D space until it touched another droplet on the superhydrophobic mesh. Due to the minimized adhesion between the droplet and the EPS sphere, the transported droplet could be easily released from the EPS sphere.

Despite the above-mentioned versatility, using the three-axis AT to transport and mix droplets has another unique advantage—the acoustic field significantly expedites the mixing process [45]. As demonstrated in Fig. 4c, when the litmus droplet was merged with the HCl droplet under the acoustic field, the color of the merged droplet quickly changed to orange and became uniformly distributed within 1 s. In contrast, in the absence of the acoustic field, the color of the merged droplet remained inhomogeneous even after 336 s (Fig. 4d, the color became homogeneous quickly upon applying the acoustic field after 336 s). Fig. 4e depicts the evolution of color inhomogeneity for the merged droplet, highlighting that the application of acoustic field resulted in much faster homogenization compared to the condition without the acoustic field. These findings underscore the crucial role of acoustic streaming inside the droplets in enhancing mixing, particularly beneficial for micro-reaction and bioassay where thorough and rapid mixing is crucial [46,47].

In fact, acoustic streaming is also observed in one-axis/two-axis acoustic fields and can be enhanced by increasing the applied voltage to the ATs (Fig. S13 in Supporting information). While acoustic streaming provides an efficient means for droplet mixing, it also accelerates droplet evaporation due to increased convective heat and mass transfer [48,49]. As demonstrated in Fig. S14 (Supporting information), the lifetime of a 1.3-μL droplet located near the center of the two-axis AT decreases from 36 min to 32 min after the acoustic field is activated (applied voltage = 30 V, temperature = 26 °C, relative humidity = 60%). Therefore, in real-world applications, special care should be taken to suppress droplet evaporation when using ATs for droplet manipulation, such as by increasing the surrounding humidity.

In summary, we have shown the feasibility of contactless manipulation of droplets on SHPSs using simple ATs. By employing an elastic fiber force sensor, we quantify the acoustic radiation forces acting on the droplets. It is found that the lateral motion of the droplet on the SHPS occurs when the acoustic radiation force surpasses the friction force. Compared to the single-axis AT, the two-axis AT is more effective and reliable for transporting droplets on the SHPSs. Droplets can be transported along any programed paths, following the motion of the two-axis AT. To address the challenge of individual manipulation of droplets amidst multiple ones using ATs, we propose incorporating distinct labyrinthine structures on the SHPS to locally confine droplets. This approach allows selective manipulation of individual droplets by transporting them out of the labyrinthine structures as needed. It is also found that the hydrophilic defect on the SHPS can be used for pinning the transported droplets, facilitating sequential mixing. Furthermore, we demonstrate the capability of using a three-axis AT to capture, transport, release and mix microliter droplets in 3D space. Internal mixing within the droplets in the acoustic field is enhanced by the acoustic streaming effect. With these capabilities for precise droplet manipulation and enhanced mixing, ATs hold signif-

icant promise for applications in bio-assay, chemical analysis and micro-reaction.

Declaration of competing interest

The authors declare that they have no known competing financial interests or personal relationships that could have appeared to influence the work reported in this paper.

CRediT authorship contribution statement

Guifeng Wen: Writing – original draft, Validation, Methodology, Investigation. **Zheyuan Zhong:** Investigation. **Yue Fan:** Methodology. **Xuelin Tian:** Supervision, Funding acquisition. **Shilin Huang:** Writing – review & editing, Supervision, Funding acquisition, Conceptualization.

Acknowledgments

The work was supported by National Natural Science Foundation of China (Nos. 12072381, 22072185, 21805315), Guangdong Basic and Applied Basic Research Foundation (No. 2024A1515011812), and Science and Technology Innovation Project of Guangzhou (No. 202102020263).

Supplementary materials

Supplementary material associated with this article can be found, in the online version, at doi:10.1016/j.cclet.2024.110672.

References

[1] J. Li, N.S. Ha, T.L. Liu, et al., Nature 572 (2019) 507–510.
[2] L. Yang, W. Li, J. Lian, et al., Science 384 (2024) 1344–1349.
[3] Z. He, H. Wu, X. Yan, et al., Chin. Chem. Lett. 33 (2022) 1729–1742.
[4] X. Han, R. Jin, Y. Sun, et al., Adv. Mater. 36 (2024) 2311729.
[5] Y. Jin, W. Xu, H. Zhang, et al., Proc. Natl. Acad. Sci. U. S. A. 119 (2022) e2105459119.
[6] G. Cheng, C.Y. Kuan, K.W. Lou, et al., Adv. Mater. 37 (2024) 2313935.
[7] L. Zhang, Z. Guo, J. Sarma, et al., Adv. Funct. Mater. 31 (2021) 2008614.
[8] H.J. Cho, D.J. Preston, Y. Zhu, et al., Nat. Rev. Mater. 2 (2016) 16092.
[9] J. Sun, L. Zhang, S. Gong, et al., Adv. Mater. 35 (2023) 2305578.
[10] J. Pipper, Y. Zhang, P. Neuzil, et al., Angew. Chem. Int. Ed. 47 (2008) 3900–3904.
[11] X. Han, S. Tan, Q. Wang, et al., Adv. Mater. 36 (2024) 2402779.
[12] Q. Sun, D. Wang, Y. Li, et al., Nat. Mater. 18 (2019) 936–941.
[13] F. Wang, M. Liu, C. Liu, et al., Sci. Adv. 8 (2022) eabp9369.
[14] H. Dai, C. Gao, J. Sun, et al., Adv. Mater. 31 (2019) 1905449.
[15] N.N. Nguyen, S. Davani, R. Asmatulu, et al., ACS Appl. Nano Mater. 5 (2022) 19017–19024.
[16] J. Hartmann, M.T. Schür, S. Hardt, Nat. Commun. 13 (2022) 289.
[17] L. Tan, Q. Zeng, F. Xu, et al., Adv. Mater. 36 (2024) 2313878.
[18] C. Yang, Q. Zeng, J. Huang, et al., Adv. Colloid Interface Sci. 306 (2022) 102724.
[19] S. Ben, T. Zhou, H. Ma, et al., Adv. Sci. 6 (2019) 1900834.
[20] Y. Huang, G. Wen, Y. Fan, et al., ACS Nano 18 (2024) 6359–6372.
[21] W.Q. Ye, W.X. Fu, X.P. Liu, et al., Chin. Chem. Lett. 35 (2024) 108494.
[22] S.K. Cho, H. Moon, C.J. Kim, J. Microelectromech. Syst. 12 (2003) 70–80.
[23] Y. Zhang, N.T. Nguyen, Lab Chip 17 (2017) 994–1008.
[24] H. Hwang, P. Papadopoulos, S. Fujii, et al., Adv. Funct. Mater. 32 (2022) 2111311.
[25] T. Luo, S. Liu, R. Zhou, et al., Lab Chip 23 (2023) 3989–4001.
[26] Z. Yuan, C. Lu, C. Liu, et al., Sci. Adv. 9 (2023) eadg2352.
[27] M. Baudoin, P. Brunet, O. Bou Matar, et al., Appl. Phys. Lett. 100 (2012) 154102.
[28] Y. Wang, Q. Zhang, R. Tao, et al., ACS Appl. Mater. Interfaces 13 (2021) 16978–16986.
[29] D. Sun, K.F. Böhringer, M. Sorensen, et al., Lab Chip 20 (2020) 3269–3277.
[30] Y. Luo, M. Zhou, L. Wang, et al., Small Methods 7 (2023) 2300592.
[31] D. Foresti, K.T. Kroll, R. Amissah, et al., Sci. Adv. 4 (2018) eaat1659.
[32] M.A.B. Andrade, N. Pérez, J.C. Adamowski, Braz. J. Phys. 48 (2018) 190–213.
[33] L.P. Gor'kov, Sov. Phys. Dokl. 6 (1962) 773.
[34] I.D. Joshipura, H.R. Ayers, G.A. Castillo, et al., ACS Appl. Mater. Interfaces 10 (2018) 44686–44695.
[35] A. Lafuma, D. Quéré, Nat. Mater. 2 (2003) 457–460.
[36] P. Papadopoulos, L. Mammen, X. Deng, et al., Proc. Natl. Acad. Sci. U. S. A. 110 (2013) 3254–3258.
[37] N. Gao, F. Geyer, D.W. Pilat, et al., Nat. Phys. 14 (2017) 191.
[38] X. Li, J. Yang, K. Lv, et al., Natl. Sci. Rev. 8 (2020) nwaa153.
[39] G. Lagubeau, M. Le Merrer, C. Clanet, et al., Nat. Phys. 7 (2011) 395–398.
[40] D. Daniel, J.V.I. Timonen, R. Li, et al., Nat. Phys. 13 (2017) 1020.
[41] M. Backholm, T. Kärki, H.A. Nurmi, et al., Proc. Natl. Acad. Sci. U. S. A. 121 (2024) e2315214121.
[42] S. Alibeigi, M.R. Vaezi, Chem. Eng. Technol. 31 (2008) 1591–1596.
[43] J.J. Sedmak, S.E. Grossberg, Anal. Biochem. 79 (1977) 544–552.
[44] D. Zang, Y. Yu, Z. Chen, et al., Adv. Colloid Interface Sci. 243 (2017) 77–85.
[45] J. Li, W.D. Jamieson, P. Dimitriou, et al., Nat. Commun. 13 (2022) 4125.
[46] Z. Chen, Z. Pei, X. Zhao, et al., Chem. Eng. J. 433 (2022) 133258.
[47] Y. Xia, J. Li, L.X. Huang, et al., Anal. Chem. 94 (2022) 6347–6354.
[48] N. Berdugo, M. Stolar, D. Liberzon, Int. J. Multiph. Flow 126 (2020) 103217.
[49] E. Bänsch, M. Götz, Phys. Fluids 30 (2018) 037103.